Photocatalytic performance of Cu$_3$SnS$_4$ (CTS)/reduced graphene oxide (rGO) composite prepared via ball milling and solvothermal approach

Anju Sebastian[1], V. Maheskumar[1,4,*], N. Bhuvanesh[3], B. Vidhya[1,2,*] , R. Nandhakumar[1,*], and Zhenyi Jiang[4]

[1] *Department of Physics, Karunya Institute of Technology and Sciences, Coimbatore 641 114, India*

[2] *Centre for Nanoscience and Genomics, Karunya Institute of Technology and Sciences, Coimbatore 641 114, India*

[3] *Department of Chemistry, Karunya Institute of Technology and Sciences, Coimbatore 641 114, India*

[4] *Shaanxi Key Laboratory for Theoretical Physics Frontiers, Institute of Modern Physics, Northwest University, Xian 710069, People's Republic of China*

ABSTRACT

A visible light-driven Cu$_3$SnS$_4$/rGO (CTS/rGO) composite photocatalyst was prepared using ball milling (B) and solvothermal (S) method. CTS prepared by both the methods was preferentially oriented along the (1 1 2) plane exhibiting a tetragonal structure. The SEM image indicates an irregular structure and flower-like appearance in the morphology of CTS samples prepared by ball milling and solvothermal process, respectively. The impact on the morphological structure of CTS by incorporating rGO in both the methods of preparation has been analysed. UV–vis-DRS shows that the incorporation of rGO effectively influences the light response performance of the composite material in visible light. The photoluminescence (PL) spectra reveal that the composite photocatalyst can either effectually detach the electron–hole pairs and curtail their recombination or enhance the recombination based on the method of preparation owing to the phase purity of the prepared sample. Degradation of the model pollutant methylene blue (MB) was used to study the photocatalytic activity of the samples. The influence of rGO incorporation on the functioning of CTS as a photocatalyst has been studied. The species trapping experiments depicted the prominent role of h$^+$ active species in the photocatalytic degradation of MB. The mechanism of photocatalysis in the presence of CTS/rGO has been discussed in detail.

Address correspondence to E-mail: mahes.ksm91@gmail.com; vidhyabhojan@gmail.com; rajunandha@gmail.com

1 Introduction

It is a known fact that, over the past few years, environmental pollution caused by several industries has gained attention as an important global problem. The main environmental pollution such as waste water effluents from textile, paper, cosmetics, food, and pharmaceuticals; fabric and plastic industries release various organic dyes and waste effluents into aqueous streams [1–4]. Recently, the development of semiconductor photocatalysts has been investigated extensively for waste water treatment [5, 6]. In recent times, copper tin sulphide (CTS) has grabbed attention as an excellent photocatalyst owing to its abundant availability, innocuous property, p-type electrical conductivity, and the energy gap ranging from 1.0 eV to 1.8 eV. Also copper tin sulphide finds applications in various fields like photovoltaics, photocatalysis, thermoelectrics, Li-ion batteries, and hydrogen evolution reaction [7–10]. For example, Chengzhi Ruan et al. have reported the application of Cu_2SnS_3 in photovoltaics and our research group has recently synthesized Cu_3SnS_4 for photocatalytic dye degradation of methylene blue (MB) and electrocatalytic hydrogen evolution reaction (HER) [11–13].

The main drawbacks of CTS include its low electrical conductivity and rapid recombination of photo-induced charge carriers. To address the above-mentioned drawbacks suitable substrate materials of good conductivity, different morphologies of CTS, high surface area, and P-N heterojunction may be used to enhance the performance. Yu Tan et al. have prepared Cu_2SnS_3 by simple solvothermal method, which shows 3D flower-like architectures, the absorption edge was observed in the visible light region and a complete degradation of MB has been observed after 4 h of irradiation [14] Yan Li et al. reported the dip coating self-assembly method to prepare Cu_3SnS_4/TiO_2 film of heterojunction which exhibited noteworthy degradation of organic pollutants under the irradiation of simulated sunlight [15]. Tao shen et al. created p-n heterojunction with nanoparticles of ZnS and porous Cu_3SnS_4 for improved degradation of methyl blue under natural sun light [16]. Various reports have mentioned that the Cu-Sn-S-based chalcogenides are alloyed in different forms such as Cu_2SnS_3, Cu_3SnS_4, Cu_4SnS_4, and Cu_2SnS_7. Among them Cu_3SnS_4 has more efficiency towards photocatalytic activity, compared to other Cu-Sn-S-based chalcogenides. Cu_3SnS_4 has a wider thermodynamic stability window in chemical potential, and also it exhibits metallic behaviour, due to high Cu:Sn ratio of 3:1 and Cu has a both $+ 1$ and $+ 2$ oxidization states that lead to high hole carrier of 10^{22} cm^{-3}, similar to CuS in electronic and structural characteristics [17–20]. Graphene, a delocalized conjugated carbon material is reported to well match with the energy levels of various photocatalysts which have attracted the preparation of composite photocatalysts using graphene-based materials [21, 22]. It exhibits large surface area and separates the excited electron hole pair at an improved rate to enhance the photocatalytic activity [23, 24].

However, there are only few reports on graphene-based copper tin sulphide composites with an outstanding photocatalytic performance. Lin et al. demonstrated the preparation of Cu_3SnS_4-supported reduced graphene oxide prepared by solvothermal method. Cu_3SnS_4/rGO showed superior photocatalytic activity than the bare Cu_3SnS_4 material exposed to visible light for the degradation of rhodamine B (RhB) and phenol, which was arising from an effective light absorption and active charge carrier separation [25]. Vadivel et al. prepared the Cu_2SnS_3 flowers/rGO nanocomposites with biomolecules aiding the solvothermal method and established it as an efficient photocatalyst for the degradation of eosin dye under the irradiation of visible light [26].

In the present investigation, the photocatalytic activity of CTS/rGO synthesized via two distinct approaches such as ball milling and solvothermal method has been systematically studied. The influence of the preparation method of CTS/rGO on the structural, morphological properties, and optical bandgap of the material has been discussed. Compared to CTS/rGO prepared by solvothermal method, ball milling method exhibited superior activity in degrading methylene blue (MB) on exposure to visible light irradiation. Furthermore, the photocatalytic mechanism has been put forward by identifying the key species in the reaction process of MB degradation.

2 Experimental details

2.1 Preparation of reduced graphene oxide (rGO)

Modified Hummers method was adopted in the preparation of Graphene oxide (GO) [27, 28]. Reduction of GO was conducted by reduction method using sodium borohydride. 100 ml of deionized water was used to disperse 0.3 g of GO under continuous sonication until a clear solution is obtained. After adding 0.4 g of sodium borohydride to this solution, the solution was subjected to heating in an oil bath. The reaction temperature was set at 100 °C for 24 h. The obtained product was thoroughly rinsed with deionized water to get the rGO sample.

2.2 Preparation of CTS and CTS/rGO by ball milling method

Starting materials for CTS include granular copper (99.90%, Sigma Aldrich), tin (99.85%, Aldrich), and sulphur (99.99%, Sigma Aldrich) in a molar ratio of 3:1:4. (Fritch premium line P-7) is the type of planetary ball mill used in the present work. The starting materials were shifted to a zirconia grinding jar and zirconia balls were added in the ratio 1:5. An optimized rotation speed of 800 rpm(rotation per minutes) was utilized. The milling time was set at 60 h. The prepared CTS and rGO were taken in the ratio 10:1 and mixed thoroughly using the above-mentioned ball mill.

2.3 Preparation of CTS and CTS/rGO by solvothermal method

The CTS/rGO composite was prepared by one-pot solvothermal method. Firstly 90 ml of ethylene glycol was taken and 3 mmol $CuCl_2.2H_2O$, 1 mmol $SnCl_2.2H_2O$, and 4 mmol thiourea were dissolved in it. The solution was subjected to continuous magnetic stirring for 30 min. Secondly, in 10 m1 ethylene glycol, 0.06 g GO was dispersed by sonicating for 30 min and a uniform suspension of exfoliated graphene oxide was obtained. The later was added to the former solution gradually. After a thorough mixing of both the solutions at room temperature for 30 min, the final solution was added in to a 100-mL Teflon-lined stainless steel autoclave and tightly sealed. It

was then kept at 180 °C for 20 h. The autoclave was then allowed to cool down naturally to room temperature. The obtained black precipitate was washed several times with deionized water and absolute ethanol to remove any unreacted impurities in the final product. Lastly, the thoroughly washed black precipitate was subjected to drying at 80 °C for 4 h in a vacuum oven. For comparison, pure CTS without the addition of GO was prepared using the same solvothermal method.

2.4 Characterization

The phase structure of the samples was characterized by powder X-ray diffractometer (Shimadzu X-600, Japan) with Cu Kα ($\lambda = 1.5416$ Å) radiation source in the range of 10° to 70°. The morphology of the obtained samples was analysed by using scanning electron microscope (SEM) JEOL 6390, Japan, where the sample was dispersed on a conducting tape. JASCO V-770 spectrometer was used to record the UV–vis NIR diffusion reflection spectra in the wavelength range from 400 to 2300 nm and the optical absorption spectra of the samples were recorded using $BaSO_4$ as reference. FLUOROLOG, HORIBA Jobin Yvon spectrophotometer equipped with a Xenon lamp, was utilized to study the room temperature photoluminescence(PL) spectra..

2.5 Photocatalyst test

The visible light-driven photocatalytic activities of CTS and CTS/rGO were measured by the degradation of methyl blue (MB) in aqueous solution. 300 W Tungsten Halogen lamp was used as the optical source. The concentration of methyl blue (MB) was taken as 20 mg L^{-1}. The pH of methyl blue (MB) was 6.5. Then the solution was placed in dark for 30 min under magnetic stirring in order to establish adsorption–desorption equilibrium. The model pollutant after the addition of the catalyst was exposed to visible light source under continuous stirring. 3 ml of above solution was extracted at regular interval of times from the initial 100 ml. The supernatant was collected for absorption analysis on a UV-Vis spectrometer (JASCO V-660 spectrometer). The absorbance of methylene blue at 663 nm was used for measuring the remaining dye concentration.

3 Results and discussion

3.1 XRD analysis

The X-ray diffraction patterns of CTS (B), CTS (B)/rGO, CTS (S), and CTS (S)/rGO prepared by ball milling and solvothermal method respectively are shown in Fig. 1. The prominent peaks at 2θ values of 28.63°, 47.70°, and 56.28°, and 28.62°, 47.44°, and 56.36° were observed for CTS (B) and CTS (S), respectively, due to the reflection from (1 1 2), (0 2 4), and (1 3 2) planes of tetragonal CTS. This pattern obtained is in agreement with the standard (JCPDS Card No. 33-0501) [29, 30]. The prominent diffraction has been identified along the (112) plane. The X-ray diffraction patterns of rGO synthesized by reduction method are shown in Fig. 1. The diffraction peaks at 2θ values of 25.22° and 43.94° are due to the reflection from (0 0 2) and (1 0 0) planes of rGO [31]. XRD analysis revealed that the phase of CTS did not change after the incorporation of rGO in ball milled CTS. This specifies that the addition of rGO ensures neither a new-fangled mineral direction nor an alteration in favoured directions of CTS(B), whereas a minority peak corresponding to the secondary phase SnS_2 in accordance with JCPDS Card No 75-0367 corresponding to (0 0 3) plane has been observed for CTS(S)/rGO. The characteristic peaks for rGO (0 0 2) diffraction at 26° and (1 1 0) peak at 44.5° were not observed in the compound, this might be due to the minute quantity and comparatively low intensity of
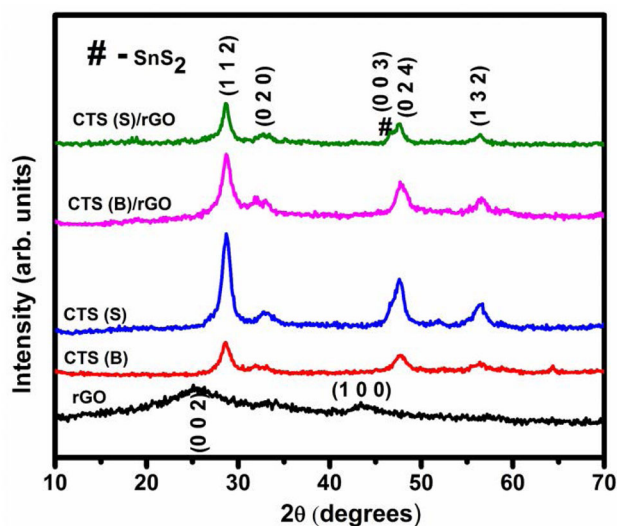
rGO. The peak intensity of CTS (S) is higher than that of CTS (B) ensuring the higher crystalline nature of CTS (S), whereas CTS (S)/rGO shows a reduction in intensity which might be owed to the reduction in crystallinity of CTS with the addition of rGO and the presence of secondary phase. The result has been contradictory for CTS (B) where the addition of rGO shows an improvement in crystallinity of CTS (B) favouring the absence of secondary impurity phases. The average crystallite size is calculated for the (1 1 2), (0 2 0), (0 2 4), and (1 3 2) planes using the Scherrer formula. The lattice constants a and c were calculated using the $1/d^2 = h^2 + k^2/a^2 + l^2/c^2$ and the values are given in Table 1. It is observed that the average dislocation density and micro-strain is higher for the samples prepared by ball milling compared to the solvothermal method.

3.2 Morphological analysis

The surface morphology of rGO, CTS (B), CTS (B)/rGO, CTS (S), and CTS (S)/rGO prepared by ball milling and solvothermal method is determined using scanning electron microscope (SEM). The obtained results are presented in Fig. 2. The reduced graphene oxide (rGO) in Fig. 2a shows nanosheets with distinct edges and wrinkled surfaces. Scanning electron micrograph of CTS (B) (Fig. 2b) demonstrates an irregular shaped strongly aggregated layered structures and has a wide distribution of particle sizes. The formation of the closely packed layered structures is owed to the repeated exposure of the particles to the stress induced by the rotating balls in the vials subjected to milling. Figure 2c shows that incorporating rGO with CTS (B) does not change the morphology obviously. In comparison with CTS (B), the particle size of CTS (B)/rGO appears to be greater, which is in agreement with improved crystallinity as observed in XRD results. CTS (S) obtained from the solvothermal method is comprised of well-dispersed microspheres with self-assembled flower-like hierarchical structure morphology. As shown in Fig. 2d, it can be noticed that by incorporating rGO with CTS (S), the flower-like hierarchical morphology was disturbed and an irregular morphology is observed as shown in Fig. 2e.

Fig. 1 XRD patterns of rGO, CTS (B), CTS (S), CTS (B)/rGO, and CTS (S)/rGO

Table 1 Structural parameters determined for CTS (B), CTS (B)/rGO, CTS (S), and CTS (S)/rGO

Samples	2θ (degree)	d-spacing (A^0)	Average crystalline size, D (nm)	Average dislocation density, δ (nm^{-2})	Average microstra-in, $\mu(m^{-1})$	Observed a and c (A^0)
Cu$_3$SnS$_4$ (JCPDS	28.49	3.13				
NO.33-0501)	33.15	2.70				$a = 5.44$
	47.46	1.91	–	–	–	
	56.02	1.64				$c = 10.75$
CTS (B)	28.63	3.11				
	32.90	2.72				$a = 5.40$
	47.70	1.90	6	23	6	
	56.28	1.63				$c = 10.72$
CTS (B)/rGO	28.55	3.12				
	32.87	2.80				$a = 5.61$
	47.65	1.90	5	33	7	
	56.30	1.63				$c = 10.90$
CTS (S)	28.68	3.10				
	32.99	2.71				$a = 5.41$
	47.44	1.91	7	18	5	
	56.36	1.63				$c = 10.58$
CTS (S)/rGO	28.55	3.12				
	32.75	2.73				$a = 5.46$
	47.50	1.91	7	19	5	
	56.27	1.63				$c = 10.94$

3.3 UV–visible DRS analysis

The optical absorption of CTS (B), CTS (S), CTS (B)/rGO, and CTS (S)/rGO was measured using UV–visible diffuse reflectance spectra as presented in Fig. 3a from which it is evidenced that CTS (B), CTS (S), CTS (B)/rGO, and CTS (S)/rGO demonstrate strong absorbance in the visible and IR region. The bandgap energies of the prepared samples are obtained from the plot of the modified Kubelka–Munk function $[F(R)h\nu]^2$ versus photon energy ($h\nu$). The results are depicted in Fig. 3b The energy bandgap of CTS (B), CTS (S), CTS (B)/rGO, and CTS (S)/rGO is 1.53 eV, 1.62 eV, 1.64 eV, and 1.30 eV, respectively, which is in close agreement with the reported results [32, 33].

3.4 Photocatalysis

The photocatalytic activity of CTS (B), CTS (S), CTS (B)/rGO, and CTS (S)/rGO samples was examined by the photodegradation of methylene blue (MB) under visible light irradiation. The absorbance spectra in the range from 550 to 700 nm for different time interval for the CTS (B), CTS (S), CTS (B)/rGO, and

CTS (S)/rGO photocatalyst are shown in Fig. 4. The main absorbance peak of MB observed around 663 nm decreases with the extension of the exposure time.

The photocatalytic degradation performance of the above photocatalysts was evaluated via the variations of MB concentrations (C/C$_0$). Figure 5 displays the results of MB degradation based on CTS(B), CTS(S), CTS(B)/rGO, and CTS(S)/rGO composite photocatalysts. It can be found that the photolysis degradation of MB in the absence of photocatalyst is negligible. After irradiation for 6 h, the concentration of MB obviously subsided with the existence of the photocatalyst. From Fig. 5a, it can be observed that when the ball milled sample CTS (B) was added into this photocatalytic system, just 78% of MB was degraded, whereas the sample prepared by solvothermal method CTS (S) shows 83% degradation of MB for the same time period. For CTS (B)/rGO, an obvious enhancement of degradation efficiency (88%) is achieved. This is in agreement with the reported results where an increase in photocatalytic degradation has been observed with the incorporation rGO in other semiconducting materials [17, 18]. In
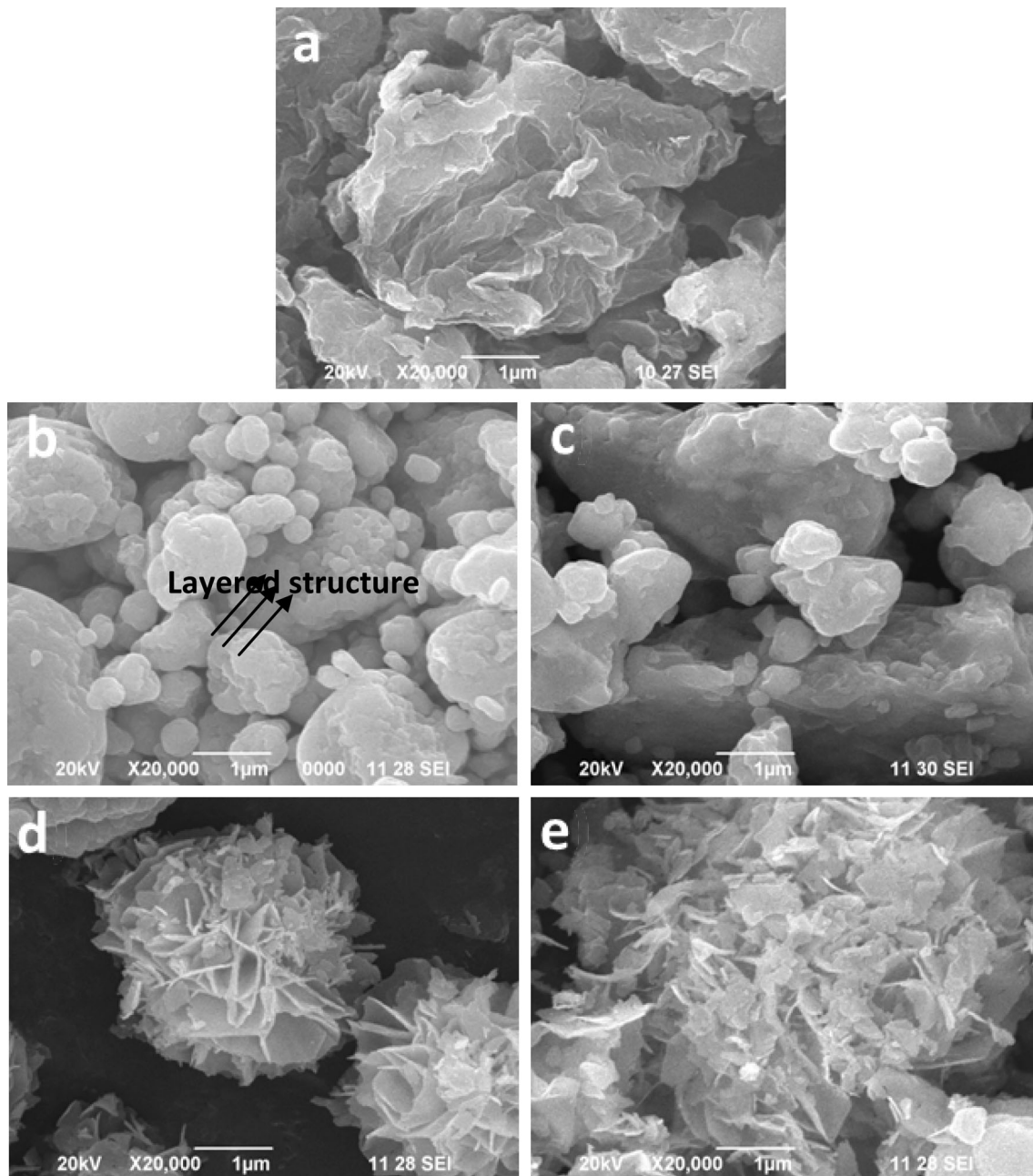
Fig. 2 Scanning electron microscope (SEM) images of **a** rGO, **b** CTS (B), **c** CTS (B)/rGO, **d** CTS (S),, and **e** CTS (S)/rGO

contradiction to these results, for CTS (S)/rGO, the photocatalytic activity has decreased to (49%). This is attributed to the impurity secondary phase present in CTS(S)/rGO as evidenced in Fig. 1 which in turn resulted in a reduced absorbance and energy gap value as shown in Fig. 3 a and b resulting in an effective usage of less photon energy as compared to the CTS(B)/rGO.

The reaction kinetics of the photocatalytic MB degradation has been reported by fitting the experimental data by the Langmuir–Hinshelwood model, as expressed by $\ln(C/C_0) = kt$, where C and C_0 are the concentrations of MB solution at time t and initial concentration, k is the first-order rate constant, respectively [34]. Figure 5b gives the kinetics of MB degradation with the rate constant of CTS (B), CTS (S), CTS (B)/rGO, and CTS (S)/rGO, respectively. CTS (B)/rGO shows a photocatalytic activity of 2.9, 1.4 and 6.8 times higher than CTS (B), CTS (S), and CTS (S)/rGO, respectively.
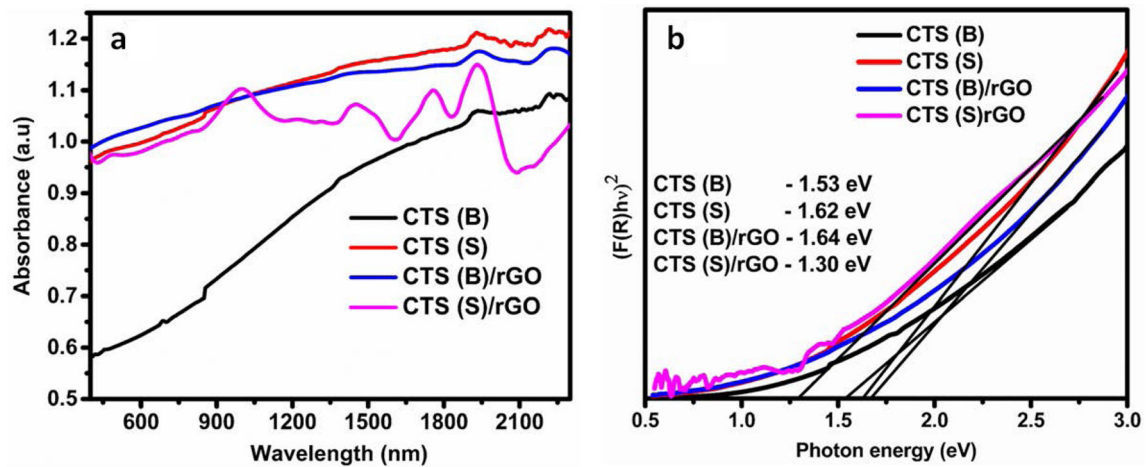
Fig. 3 **a** UV–vis NIR absorption spectra of CTS (B), CTS (S), CTS (B)/rGO and CTS (S)/rGO. **b** Tauc plot of CTS (B), CTS (S), CTS (B)/rGO, and CTS (S)/rGO
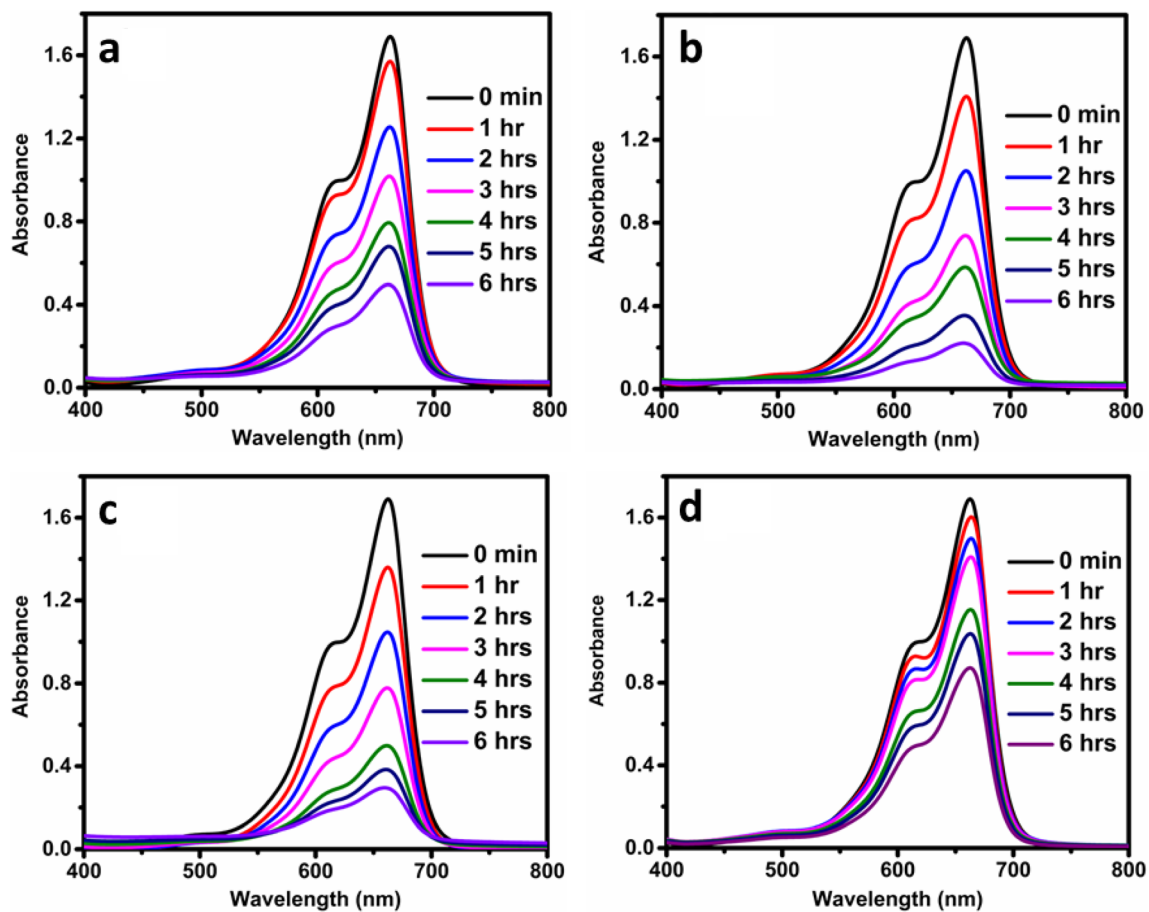

Fig. 4 UV–vis absorption spectra of MB dye in the presence of, **a** CTS (B), **b** CTS (S), **c** CTS (B)/rGO, and **d** CTS (S)/rGO for different time intervals
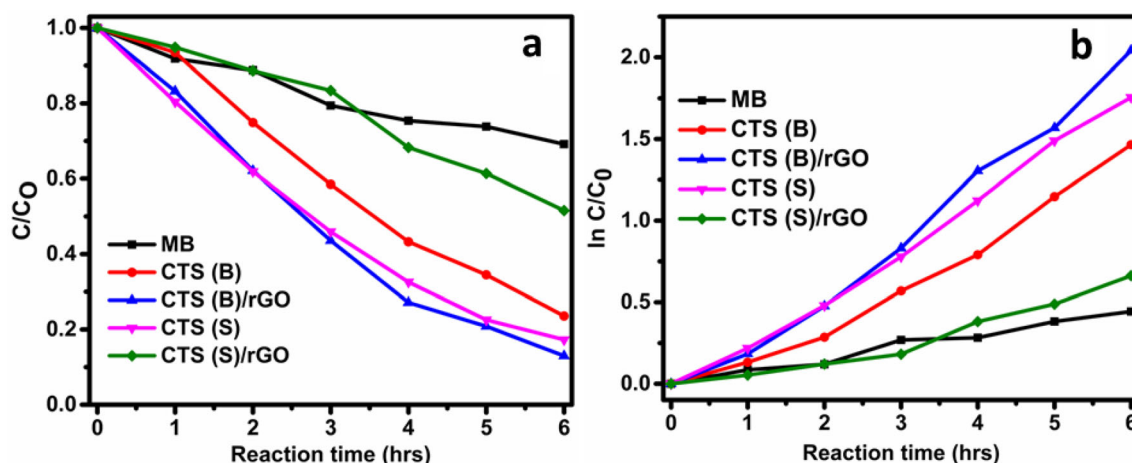
Fig. 5 **a** MB photocatalytic degradation in the presence of CTS (B), CTS (S), CTS (B)/rGO, and CTS (S)/rGO. **b** Pseudo-first-order kinetic model fit for the degradation of MB with CTS (B), CTS (S), CTS (B)/rGO, and CTS (S)/rGO

3.5 Photoluminescence analysis

Photoluminescence spectroscopy (PL) has been generally applied to study the efficiency of the charge carrier trapping and migration and understand the successful separation rate of photogenerated positive and negative charge carriers. In general, the weaker PL intensity implies a lower probability of recombination of electron–hole pairs hence resulting in higher photocatalytic degradation activity [35, 36]. The PL spectra of CTS (B), CTS (B)/rGO, CTS (S), and CTS (S)/rGO samples are displayed in Fig. 6. All the samples show emission between 350 and 450 nm. At the same time, photoluminescence analysis shows that there are two peaks in all the samples. But this is prominent only in CTS(S)/rGO. With the addition of rGO, a shift in emission spectra towards the higher wavelength has been observed which is in accordance with the reported results. Also the shift is more pronounced in CTS(B)/rGO which is attributed to the strain induced during the milling process. Among CTS(S) and CTS(B), the later holds the maximum recombination owed to the maximum possibility of defect formation during the process of ball milling compared to CTS(S).The intensity of PL spectra of CTS (B) is decreased by incorporating rGO. The CTS (S) sample showed significantly dropped PL intensity when compared to CTS (B) and CTS (B)/rGO photocatalyst, which suggests that the unique flower morphology of CTS (S) favours the separation rate of photogenerated electron hole pairs. Besides, the lower PL intensity of CTS (B)/rGO suggests that the recombination of the photogenerated electron–hole pairs is efficiently inhibited in CTS (B) and rGO interface and the charge carrier separation rate is promoted. rGO has higher electrical conductivity, which makes it an outstanding electron-transport material in the photocatalytic process. The photogenerated electrons of excited CTS are moved promptly from the conduction band of CTS to rGO, ensuring a minimalized charge recombination and contribute to an improved photocatalytic activity. Liu et al. [25] have reported the synthesis of CTS/rGO where they have also reported the disturbance of flower-like morphology by incorporating rGO with CTS by solvothermal method and the reduction in

Fig. 6 Photoluminescence spectra of CTS (B), CTS (B)/rGO CTS (S), and CTS (S)/rGO at room temperature

bandgap compared to CTS(S) which is in accordance with our results as evidenced in Fig. 3b. But in the present work by incorporating rGO with CTS (S), the PL intensity significantly increased, which is owed to the presence of minority impurity phase of SnS_2.

3.6 Radical test

It is well known that the photocatalytic degradation processes are attributed to the photogenerated holes (h+) and free radical such as superoxide radicals (O_2^-) and hydroxyl radicals (OH) [37]. To further identify the prominent species for photo degradation of MB over the CTS (B)/rGO photocatalyst in the reaction system, we have used the scavengers ethylenediamine tetraacetate (EDTA 1 mM), iso-propyl alcohol (IPA 1 mM), and p- benzoquinone (BQN 1 mM) for the estimation of the roles of h+, .OH, and .O_2-, respectively. As shown in Fig. 7, reaction kinetic constants for the process with and without the relevant scavengers were examined. From Fig. 7, it is clear that the addition of IPA and BQN slightly affects the degradation rate of MB over the CTS (B)/rGO heterostructure, therefore .OH and.O^{2-} reactive species are to some extent involved in the photocatalytic activity. On the other hand, EDTA could completely terminate the degradation reaction rate by consuming h^+ radicals that play a major role in the photocatalysis.
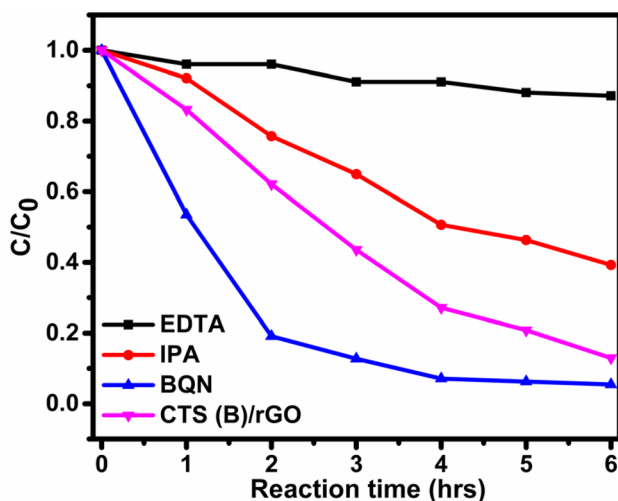
3.7 Photocatalytic mechanism

On analyses of the above results, the possible photocatalytic mechanism of CTS (B)/rGO has been proposed as shown in Fig. 8. The CTS catalyst can be activated by visible light due to its considerably higher absorbance in the visible light wavelength region as seen in Fig. 3a and its bandgap value of 1.53 eV. Upon the absorption of irradiated visible light by the CTS(B)/rGO photocatalyst, the valence band electrons are stimulated and transferred to conduction band utilizing the excess energy compared to its bandgap. This results in the electron–hole pair generation, which in turn helps in regulating the photocatalytic process. When the photo-excited electron–hole pair recombines, there is a reduction in catalytic activity. To curtail the recombination, reduced graphene oxide favours the mobility of charge carriers at room temperature; as a consequence, there is an enhanced transfer and separation of photogenerated electrons. The electron seized by the rGO reacts with O_2 to from O_2- while holes in CTS generate OH radicals. Thus under visible light source, using CTS/rGO catalyst, large amount of OH radicals and superoxide ion are generated, which enhances the degradation of the MB molecule to CO_2, H_2O owing to their strong oxidizing ability. The proposed mechanism of the probable electron movements from the conduction band of CTS to rGO is described as follows:
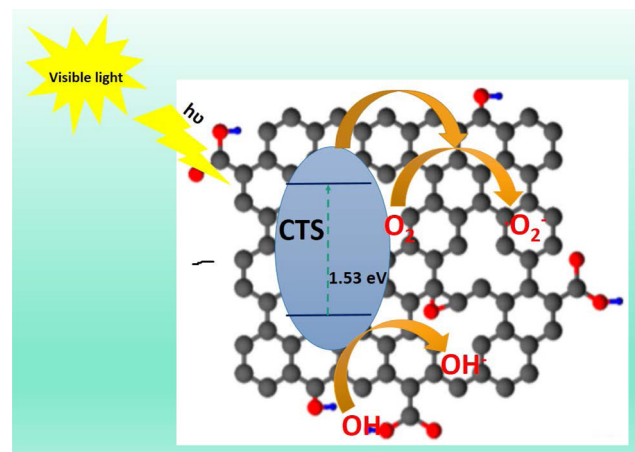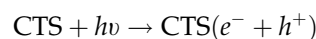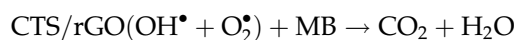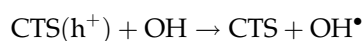
$$CTS + h\upsilon \rightarrow CTS(e^- + h^+)$$

Fig. 7 Radical species trapping experiments of photocatalytic degradation of MB over CTS (B)/rGO
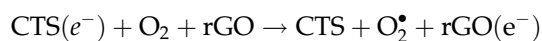

Fig. 8 Mechanism of the photocatalytic process for the CTS (B)/rGO under visible light irradiation

$$H_2O + h^+ \rightarrow OH^\bullet + h^+$$

$$OH + h^+ \rightarrow OH^\bullet$$

$$O_2 + e^- \rightarrow O_2^\bullet$$

$$CTS(e^-) + O_2 + rGO \rightarrow CTS + O_2^\bullet + rGO(e^-)$$

$$CTS(h^+) + OH \rightarrow CTS + OH^\bullet$$

$$CTS/rGO(OH^\bullet + O_2^\bullet) + MB \rightarrow CO_2 + H_2O$$
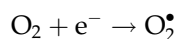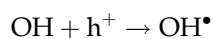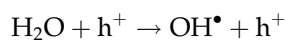
4 Conclusions

Two different methods viz via ball milling and solvothermal were adopted in the preparation of CTS/rGO composite. The photocatalytic efficiency of prepared samples was investigated by studying the degradation of MB. A noteworthy augmentation in the performance of CTS as a photocatalyst was observed in the presence of rGO for the ball milled sample. The results shows that excellent photocatalytic activity with ball milling method is due to the formation of composite between the CTS and rGO, and the composite effectively hinders the recombination of electrons and holes. Whereas for CTS (S), there is a change in flower-like morphology to uneven structures. Also secondary impurity phase of SnS_2 was observed and the energy bandgap of CTS(S)/rGO was reduced resulting in a greater probability of carrier recombination and hence a reduction in photocatalytic activity. Thus, we conclude that even with the incorporation of rGO aimed at reduction in recombination, the presence of secondary phases with respect to the preparatory methods of the sample plays a significant role. The experiments on entrapping the active species ensured that h+ plays a major role in aiding the degradation of MB on exposure to visible light radiation.

Compliance with ethical standards

Conflict of interest The authors declare that they have no conflicts of interest.

References

1. V. Augugliaro, M. Litter, L. Palmisano, J. Soria, J. Photochem. Photobiol. C Photochem. Rev. **7**, 127 (2006)
2. E. Selli, Phys. Chem. Chem. Phys. **4**, 6123 (2002)
3. Y. Paz, Appl. Catal. B Environ. **99**, 448 (2010)
4. A. Ajmal, I. Majeed, R.N. Malik, H. Idriss, M.A. Nadeem, RSC Adv. **4**, 37003 (2014)
5. S.C. Yan, S.B. Lv, Z.S. Li, Z.G. Zou, Dalt. Trans. **39**, 1488 (2010)
6. S. Khanchandani, S. Kumar, A.K. Ganguli, A.C.S. Sustain, Chem. Eng. **4**, 1487 (2016)
7. V.R. Minnam Reddy, M.R. Pallavolu, P.R. Guddeti, S. Gedi, K.K. Yarragudi Bathal Reddy, B. Pejjai, W.K. Kim, T.R.R. Kotte, C. Park, J. Ind. Eng. Chem. **76**, 39 (2019)
8. A.C. Lokhande, K.V. Gurav, E. Jo, C.D. Lokhande, J.H. Kim, J. Alloys Compd. **656**, 295 (2016)
9. Y. Guo, X. Yin, Y. Yang, W. Que, RSC Adv. **6**, 104041 (2016)
10. U.V. Ghorpade, M.P. Suryawanshi, S.W. Shin, I. Kim, S.K. Ahn, J.H. Yun, C. Jeong, S.S. Kolekar, J.H. Kim, Chem. Mater. **28**, 3308 (2016)
11. C. Ruan, J. Tao, C. Zhu, C. Chen, J. Mater. Sci. **29**, 12824–12829 (2018)
12. V. Maheskumar, T. Selvaraju, B. Vidhya, Int. J. Hydrogen Energy **43**, 22861 (2018)
13. V. Maheskumar, P. Gnanaprakasam, T. Selvaraju, B. Vidhya, J. Electroanal. Chem. **826**, 38 (2018)
14. Yu. Tan, Z. Lin, W. Ren, W. Long, Y. Wang, X. Ouyang, Mater. Lett. **89**, 240–242 (2012)
15. Y. Li, Y. Chang, H.-M. Yang, F.-T. Liu, H.-X. Zhang, C.-W. Wang, Mater. Lett. **225**, 37–41 (2018)
16. T. Shen, G. Liu, L. Wei, Y. Zhu, S. Sun, Mater. Lett. **253**, 446 (2019)
17. P. Zawadzki, L.L. Baranowski, H. Peng, E.S. Toberer, D.S. Ginley, W. Tumas, A. Zakutayev, S. Lany, Appl. Phys. Lett. **103**, 1 (2013)
18. Y. Yang, P. Ying, J. Wang, X. Liu, Z. Du, Y. Chao, J. Cui, J. Mater. Chem. A **5**, 18808 (2017)
19. S.L. Chen, J. Tao, H.B. Shu, H.J. Tao, Y.X. Tang, Y.Z. Shen, T. Wang, L. Pan, J. Power Sources **341**, 60 (2017)

20. M. Thripuranthaka, N. Sharma, T. Das, S. Varhade, S.S. Badadhe, M.O. Thotiyl, M. Kabir, S. Ogale, Adv. Mater. Interfaces **5**, 1 (2018)

21. B. Tang, H. Chen, H. Peng, Z. Wang, W. Huang, Nanomaterials **8**, 27 (2018)

22. S.G. Babu, R. Vinoth, D. Praveen Kumar, M.V. Shankar, H.L. Chou, K. Vinodgopal, B. Neppolian, Nanoscale **7**, 7849 (2015)

23. J. Sun, S. Du, RSC Adv. **9**, 40642 (2019)

24. M. Khan, M.N. Tahir, S.F. Adil, H.U. Khan, M.R.H. Siddiqui, A.A. Al-Warthan, W. Tremel, J. Mater. Chem. A **3**, 18753 (2015)

25. H. Liu, Z. Chen, Z. Jin, Y. Su, Y. Wang, Dalt. Trans. **43**, 7491 (2014)

26. S. Vadivel, D. Maruthamani, B. Paul, S.S. Dhar, A. Habibi-Yangjeh, S. Balachandran, B. Saravanakumar, A. Selvakumar, K. Selvam, RSC Adv. **6**, 74177 (2016)

27. D.J. Dmonte, A. Pandiyarajan, N. Bhuvanesh, S. Suresh, R. Nandhakumar, Mater. Lett. **227**, 154 (2018)

28. L. Shahriary, A.A. Athawale, Int. J. Renew. Energy Environ. Eng. **02**, 58 (2014)

29. V. Maheskumar, B. Vidhya, J. Photochem. Photobiol. A Chem. **356**, 521 (2018)

30. F. Chen, J. Zai, M. Xu, X. Qian, J. Mater. Chem. A **1**, 4316 (2013)

31. H. Saleem, M. Haneef, H.Y. Abbasi, Mater. Chem. Phys. **204**, 1 (2018)

32. X. Lin, A. Steigert, M.C. Lux-Steiner, A. Ennaoui, RSC Adv. **2**, 9798 (2012)

33. Y. Li, Y. Chang, F.T. Liu, Y. Zhao, J. Wang, C.W. Wang, Mater. Des. **133**, 426 (2017)

34. Y. Guo, J. Li, Z. Gao, X. Zhu, Y. Liu, Z. Wei, W. Zhao, C. Sun, Appl. Catal. B Environ. **192**, 57 (2016)

35. S. Kumar, C.M.A. Parlett, M.A. Isaacs, D.V. Jowett, R.E. Douthwaite, M.C.R. Cockett, A.F. Lee, Appl. Catal. B Environ. **189**, 226 (2016)

36. S. Talukdar, R.K. Dutta, RSC Adv. **6**, 928 (2016)

37. Z. Zhang, S. Lin, X. Li, H. Li, W. Cui, RSC Adv. **7**, 56335 (2017)